Article

Synthesis and Application of MnO-Fe$_2$O$_3$ Nanocomposites for the Removal of ^{137}Cs and ^{60}Co Radionuclides from Artificial Radioactive Aqueous Waste

Hosam M. Saleh [1,*] , **Hazem H. Mahmoud** [1,*] , **Refaat F. Aglan** [2] **and Mohamed M. Shehata** [3]

[1] Radioisotope Department, Nuclear Research Center, Egyptian Atomic Energy Authority (EAEA), Cairo 11787, Egypt
[2] Department of Analytical Chemistry, Hot Labs Center, Atomic Energy Authority, Cairo 11787, Egypt
[3] National Center of Radiation Research and Technology, Atomic Energy Authority, Cairo 11787, Egypt
[*] Correspondence: hosam.saleh@eaea.org.eg or hosamsaleh70@yahoo.com (H.M.S.); hazem_h_mansour@yahoo.com (H.H.M.); Tel.: +20-1005191018 (H.M.S.); Fax: +20-2-37493042 (H.M.S.)

Abstract: For innovative application in wastewater treatment techniques, MnO-Fe$_2$O$_3$ nanocomposites were successfully synthesized using the sol–gel auto-combustion method at different temperatures for the adsorption of ^{137}Cs and ^{60}Co radionuclides from aqueous solution. The characterization of these nanocomposites was carried out through FT-IR, SEM-EDX, and X-ray diffraction. These nanocomposites were employed as adsorbent materials for the removal of ^{137}Cs and ^{60}Co radionuclides from simulated radioactive waste solutions. The study involved a series of experiments aiming to demonstrate the MnO-Fe$_2$O$_3$ nanoparticles' exceptional adsorption potential concerning ^{137}Cs and ^{60}Co. Additionally, the investigation delved into how variations in temperature, dose amount, contact time, and pH value influence the adsorption dynamics. Due to their high specific surface area, the synthesized MnO-Fe$_2$O$_3$ nanoparticles had high adsorption capacity of more than 60% and 90% for ^{137}Cs and ^{60}Co, respectively. By investigation of kinetics and adsorption isotherms, pseudo-second-order reaction and the Langmuir model turned out to fit well for the adsorption of ^{137}Cs and ^{60}Co onto the MnO-Fe$_2$O$_3$ nanocomposites. Moreover, a thermodynamic analysis revealed that the adsorption process was spontaneous for both target metals and the adsorption of ^{60}Co was endothermic, whereas the adsorption of ^{137}Cs was exothermic.

Keywords: MnO-Fe$_2$O$_3$ nanocomposites; radioisotopes; adsorption; sol–gel auto-combustion method; ^{137}Cs; ^{60}Co

1. Introduction

Nowadays, the development of contemporary and advanced methods for wastewater treatment is of significant relevance and a hot issue of current scientific research all over the world in order to deal with steadily increasing environmental concerns [1]. In recent years, there has been increased interest in using magnetic particles to alleviate various environmental challenges. Radioactive waste and nuclear pollution primarily originate from nuclear fuel-based electricity generation, nuclear weaponry testing, fuel reprocessing, and nuclear incidents [2], as well as the use of radionuclides in medicine, agriculture, industry, and research. This radioactive waste has a negative impact on human health and the environment [3]. Furthermore, the extensive distribution of radionuclides in the environment has led to the inclusion of liquid radioactive waste from diverse civil nuclear applications and nuclear facilities among hazardous materials [4].

The most significant procedure in the management of radioactive waste is treatment, which tries to concentrate and reduce waste produced in order to ensure safety and to lower the costs of following management schemes. Liquid radioactive waste is regarded as having a highly hazardous effect on humans and the environment, highlighting the critical

need for evaluating and improving its treatment around the world [5]. The choice of its many management alternatives is due to the need for shielding, the radioactivity level in the waste influences. Therefore, the current, widely accepted classification system is based on the amount of activity and half-life.

Several alternative approaches to the elimination of heavy metals and radionuclides from contaminated aqueous systems have been investigated. Coagulation, chemical precipitation, ion exchange, adsorption, solvent extraction, membrane filtration, phytoremediation, and liquid membrane techniques are examples of these approaches [6].

Liquid radioactive waste can be categorized as easily detectable high-energy gamma-ray emitters; numerous investigations into enhancing their treatment [7,8], immobilization [9,10], and isolation [11] from the environment have been reported.

Particularly, radionuclides like ^{137}Cs and ^{60}Co, components of low-level radioactive waste (LLRW), pose significant risks to human well-being due to their capacity for efficient transfer, high solubility, extended half-lives, and propensity to accumulate in living organisms [12]. ^{137}Cs and ^{60}Co are used in irradiation and for investigating the sensitivity of dosimeters [13,14].

Cesium has a high water solubility and easily spreads in the surrounding environment [15], while cobalt is a corrosive, toxic element and seriously affects the environment [16]. The contamination of soil and water by the common fission product radionuclides, namely, ^{137}Cs and ^{60}Co, leads in prolonged radiation and subsequent probable contamination of the food chain, posing an environmental concern to human health [17]. Given these attributes, it is crucial to eliminate ^{137}Cs and ^{60}Co from waste streams prior to releasing them into the environment. Over the years, a range of distinct techniques have been developed for treatment purposes, such as chemical precipitation, solvent extraction, reverse osmosis, ion exchange, and adsorption [18], with adsorption being widely adopted to remove heavy metals from contaminated water.

A growing fascination within the scientific realm centers on the development of innovative nanoscale composite materials that incorporate various metal oxides. This focus is particularly geared towards tackling pressing environmental issues, including the elimination of harmful dyes and metal ions from water matrices. These nanoscale composites, comprising multiple metal oxides, not only retain the advantages of their individual constituents but also exhibit synergistic effects that enhance the overall physicochemical properties of the composite [19,20]. The production of nanoscale multi-metal oxides has been successfully accomplished using a variety of ceramic processing methods, encompassing precipitation, sol–gel, and hydrothermal pathways [21,22]. Among these, the sol–gel approach stands out due to its simplicity, cost-effectiveness, well-established, flexible synthetic route, and environmentally benign nature [23].

One such composite is the MnO-Fe$_2$O$_3$ nanocomposite. The MnO-Fe$_2$O$_3$ composite can easily be prepared and has been proven to be a low-cost material [1]; however, in this study, synthetic MnO-Fe$_2$O$_3$ nanocomposites were produced using the sol–gel auto-combustion technique. The physicochemical attributes of these nanocomposites were thoroughly assessed. The primary objectives encompassed an exploration of the influence of initial metal ion concentrations, initial solution pH, and temperature on the capacity of synthetic MnO-Fe$_2$O$_3$ nanocomposites to remove ^{137}Cs and ^{60}Co from their aqueous solutions. The underlying adsorption mechanisms were also subjected to kinetic and thermodynamical investigations. The insights garnered from this study concerning the adsorption of ^{137}Cs and ^{60}Co onto MnO-Fe$_2$O$_3$ nanocomposites under varying conditions offer valuable input for addressing the challenges posed by low-level radioactive waste (LLRW). Thus, the objective of the presented work was to assess the removal effectiveness of MnO-Fe$_2$O$_3$ nanocomposite for ^{137}Cs and ^{60}Co under various conditions.

2. Experiments

2.1. Chemicals

All chemicals employed in the experiments were of analytical reagent (AR) grade (99.9% purity) and were utilized without undergoing any purification processes. This includes manganese (II) sulphate pentahydrate ($MnSO_4 \cdot 5H_2O$), ferrous sulphate hexahydrate ($FeSO_4 \cdot 6H_2O$), citric acid, and ethylene glycol, purchased from Merck.

2.2. Preparation of MnO-Fe$_2$O$_3$ Nanocomposite

The process of sol–gel involves forming a colloidal suspension termed as a sol, which subsequently transforms into a solid three-dimensional structure within a continuous liquid medium, leading to the formation of a gel. These colloids are typically composed of a metal or metalloid element enclosed by different reactive compounds. To initiate the process, $MnSO_4 \cdot 5H_2O$ and $FeSO_4 \cdot 6H_2O$ were dissolved in distilled water, employing predetermined stoichiometric ratios, and then agitated for 15 min on a heated plate furnished with a magnetic stirrer. Subsequently, a chosen precipitating agent was carefully introduced in a drop-wise manner. The resulting precipitates were separated through filtration and left to desiccate for a duration of one night at 110 °C. The resultant precipitate was amalgamated with an aqueous solution of citric acid, and this mixture was then dissolved by gradually adding concentrated nitric acid. In this context, citric acid functioned as the fuel while nitric acid acted as the oxidizer during the combustion process. The ultimate step involved adjusting the pH value to 7, a level that facilitates improved complexation of the metal ions [24]. This pH adjustment was realized by incorporating a 25 vol% aqueous ammonia solution. Following this, the sols were subjected to heat until a gel-like structure emerged, which was subsequently pulverized to obtain a uniform powder. The final product underwent calcination at temperatures of 500, 800, and 1100 °C for a period of 4 h each.

2.3. Preparation of Radioactive Waste Solutions

For the creation of radioactive waste solutions, two radioisotopes, namely ^{137}Cs and ^{60}Co, were procured from the Institute of Atomic Energy, POLATOM, Poland. A radioactivity of 127 MBq/mL and a purity exceeding 99.5% were achieved for CsCl, which represented the ^{137}Cs source. Similarly, $CoCl_2$, containing ^{60}Co, had a radioactivity of 115 MBq/mL with a purity exceeding 99%. These activities were then appropriately diluted to suitable levels for experimental purposes.

Diverse aqueous solutions, characterized by varying initial radioactivity and ascending pH values, were meticulously prepared. Subsequently, these solutions underwent the remediation process using the designated equipment. Diluted solutions of HNO_3 or NaOH were employed to establish media with predefined pH values.

2.4. Techniques for Characterization of Adsorbent

X-ray diffraction (XRD) patterns were generated using a powder X-ray diffractometer (BRUKER D8 Advance, Billerica, MA, USA) equipped with a Cu target and a wavelength of 1.54 Å, operating at 40 kV and 40 mA, from Germany. Surface morphology and compositional analysis of the films were observed utilizing a scanning electron microscope (JEOL JSM6360, Peabody, MA, USA) at an operational voltage of 20 kV. Fourier transform infrared (FT-IR) spectra were acquired via an FT-IR spectrophotometer (Nicolet is 10 spectrometer, Rhinelander, WI, USA), covering the range of 4000–400 cm^{-1} with a resolution of 2 cm^{-1}, employing KBr pellets at room temperature. The progression of the adsorption process was tracked by measuring the remaining activity content within the solutions, employing a multichannel analyzer connected to a NaI detector (PCAP, Wilmington, DE, USA).

2.5. Conducting Adsorption Experiments

To assess the highest adsorption capacity of MnO-Fe$_2$O$_3$ nanocomposites for ^{137}Cs and ^{60}Co, the experimental outcomes were processed employing the following Equation (1):

$$\text{Uptake\%} = \frac{\text{initial activity of waste solution} - \text{remaining activity in waste solution}}{\text{initial activity of waste solution}} \times 100 \qquad (1)$$

Thermodynamic parameters pertinent to the adsorption mechanisms of ^{137}Cs and ^{60}Co onto MnO-Fe$_2$O$_3$ nanocomposites were computed.

The influence of solution pH value was explored across a pH range spanning from 2 to 12, maintaining a temperature of 25 °C. For each test, 50 mL of a solution containing both ^{137}Cs and ^{60}Co was introduced into a 50 mL conical centrifuge tube made of polyethylene (SPL Labware, Pocheon-si, Republic of Korea). Subsequently, these solutions were mixed with 0.2 g of MnO-Fe$_2$O$_3$ nanocomposites. The initial pH of the solutions was tailored by adding either 0.1 N HNO$_3$ or 0.1 N NaOH solution. The resulting suspensions were subjected to agitation in a rotary shaker, set at 200 rpm, for a duration of 24 h. Subsequently, these mixtures underwent filtration using a 0.2 mm pore size syringe filter, after which they were analyzed for their final pH values and the concentration of metal ions. The pH measurement was carried out using a pH meter (Thermo Orion, model 720A+, Waltham, MA, USA).

3. Results and Discussion

3.1. Characterization of MnO-Fe$_2$O$_3$ Nanocomposite

3.1.1. Surface Morphology and Composition Analysis via SEM-EDX

The morphology of MnO-Fe$_2$O$_3$ nanocomposites synthesized at different temperatures can describe the degree of interaction between the sorbent and the metal ion species. The morphological structure and surface properties of MnO-Fe$_2$O$_3$ nanocomposites were examined using scanning electron microscopy (SEM). The results are depicted in Figure 1, which show a rough surface, and the presence of a uniformly porous structure nanocomposite on a large scale [25]. The surface area and porous structure of the produced nanocomposite will play an important role in the adsorption process.
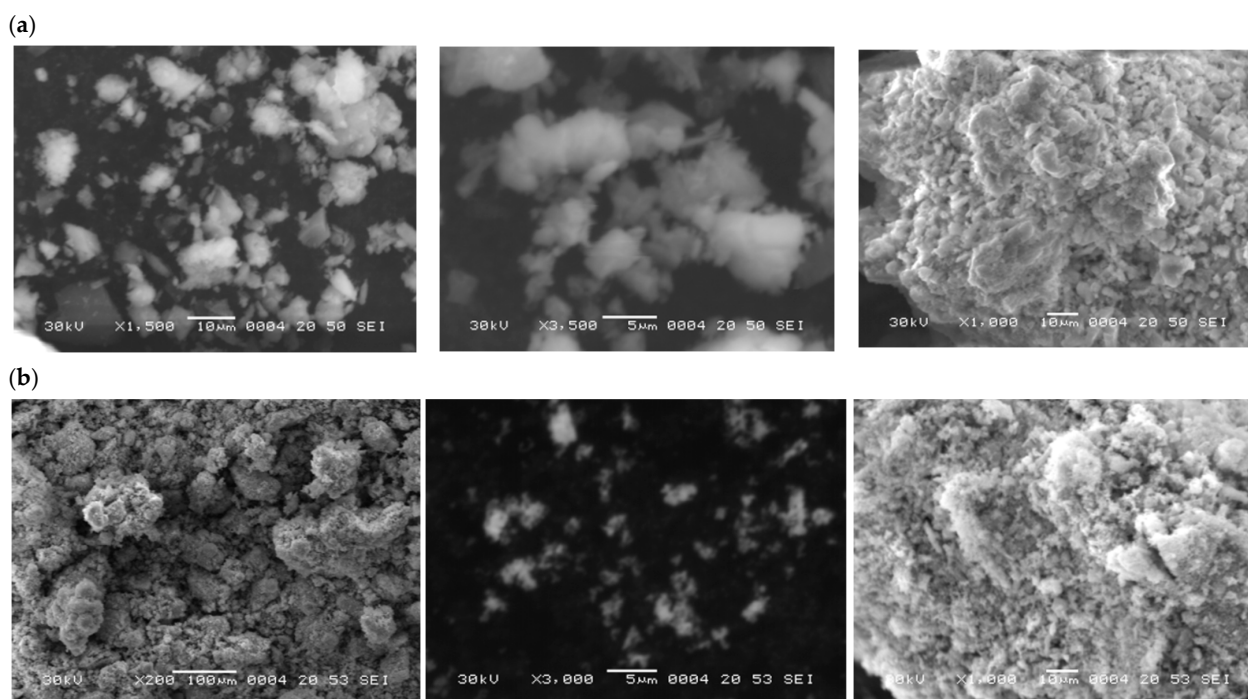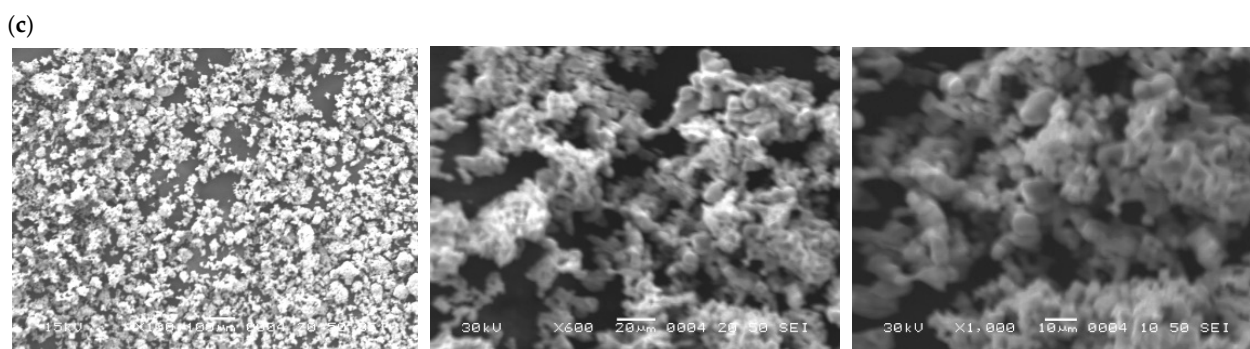
(a)

(b)

Figure 1. *Cont.*

(**c**)

Figure 1. Scanning electron microscopy (SEM) images of the MnO-Fe$_2$O$_3$ nanocomposites synthesized at (**a**) 500 °C, (**b**) 800 °C, and (**c**) 1100 °C.

To establish the composition of the composite oxide, energy-dispersive X-ray (EDX) analysis was performed. In the EDX spectrum illustrated in Figure 2, the spectral lines identified in this EDX analysis align consistently with the outcomes documented in other sources [26]. A quantitative assessment derived from the EDX data determined the elemental percentages within the matrix, including their energy distribution. This analysis method enabled the direct determination of the composition of the examined samples such as iron based on the EDX data.
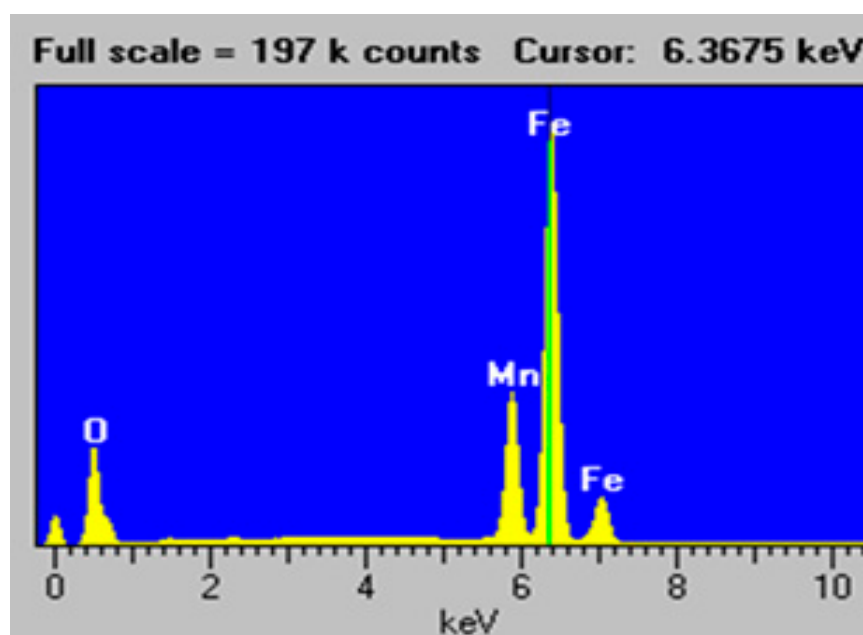

Figure 2. EDX spectrum of the synthesized MnO-Fe$_2$O$_3$ nanocomposites.

3.1.2. Analysis of X-ray Diffraction (XRD)

X-ray diffraction was used to determine the formed structure of the produced nanocomposites at three selected temperatures. Figure 3 illustrates a representative XRD pattern of the synthesized MnO-Fe$_2$O$_3$ nanocomposites under optimized conditions, conclusively affirming the identity of the synthesized sample as MnO-Fe$_2$O$_3$ nanocomposites. Furthermore, the XRD patterns obtained for the synthesized samples demonstrate variations resulting from calcination at distinct temperatures (500, 800, and 1100 °C). Observing the XRD pattern at 500 °C, the conspicuous elevated background within the diffraction spectra of both samples signifies the presence of an amorphous phase within the resultant materials.
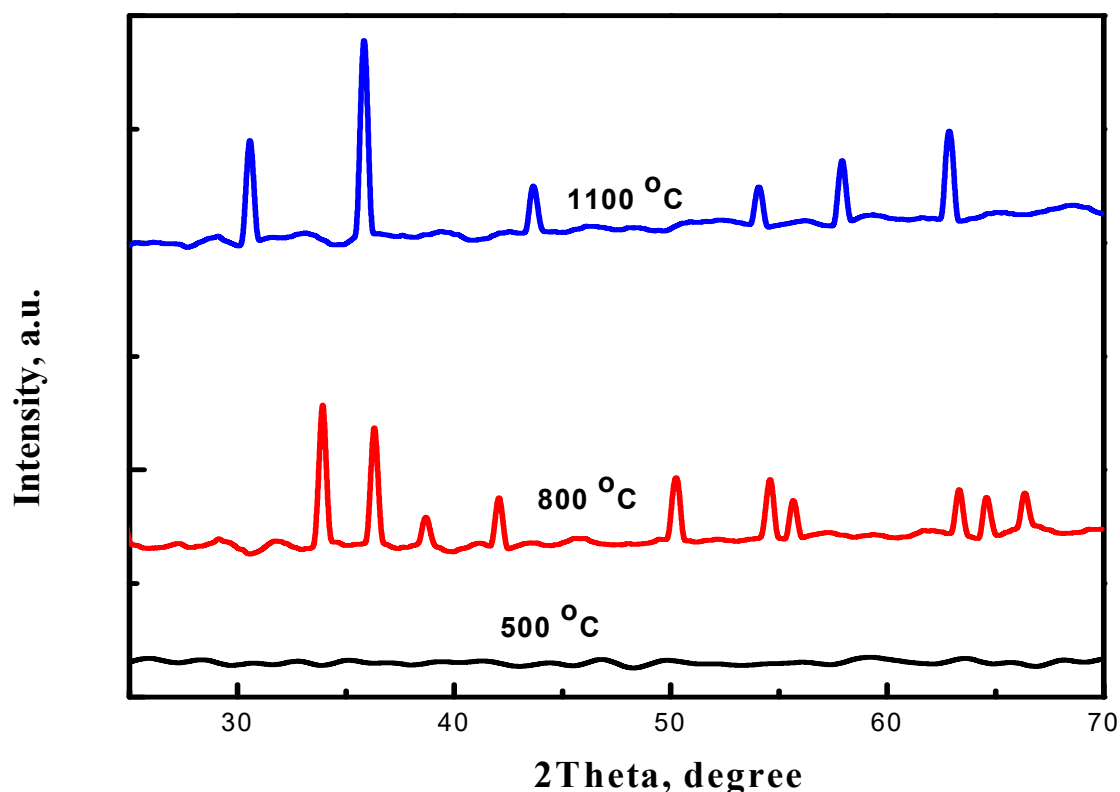
Figure 3. X-ray diffraction (XRD) patterns of synthesized MnO-Fe$_2$O$_3$ nanocomposite at 500, 800, and 1100 °C.

As for the XRD pattern at 800 °C, the distinctive diffraction pattern unveils lines characteristic of Fe$_2$O$_3$. Upon reaching 1100 °C, the XRD pattern distinctly reveals lines corresponding to the cubic phase of either MnFe$_2$O$_4$ or MnO-Fe$_2$O$_3$, thereby indicating a transformation in the material's crystalline structure. The diffraction peaks of Mn$_2$O$_3$ nanoparticles were assigned at 31°, 38.2 °, 44.1°, 56°, and 63.7°, while the diffraction peaks of Fe$_2$O$_3$ nanoparticles were assigned at 36.6°, 50.1°, 54.1°, 57.6° and 64.0° [27]. This assertion was substantiated by Fourier transform infrared (FTIR) analysis, as described in the following Section 3.1.3.

3.1.3. FTIR Analysis

FTIR spectroscopy was employed in the range of 4000–400 cm^{-1} to investigate the surface of the nano-adsorbents, enabling insights into the chemical bonds present on the surface materials, as shown in Figure 4. The broad band at 3340 cm^{-1} was attributed to the O–H stretching vibrations of hydroxyl groups or adsorbed water molecules, while the band at 1625 cm^{-1} confirmed the presence of adsorbed water molecules at low temperatures only [28].

At all temperatures, the noticeable bands centered at 473 and 541 cm^{-1} are attributed to the mixed oxides associated with the stretching vibrations of M-O (Mn–O/Fe–O bonds in the MO$_4$ tetrahedron and MO$_6$ octahedron, respectively) [29].

3.2. Adsorption Studies

3.2.1. Impact of Calcination Temperature on Radioisotope Adsorption by Nanocomposites

The adsorption capacity of synthesized MnO-Fe$_2$O$_3$ nanocomposites prepared under different calcination temperatures has been performed as a preliminary test to evaluate the optimal calcination temperature that produces the most efficient adsorbent. As shown in Figure 5, the MnO-Fe$_2$O$_3$ nanocomposite prepared under higher calcination temperature had a higher adsorption capacity of ^{137}Cs than the others prepared through at a lower

temperature. The higher the calcination temperature, the higher the crystallinity and the lower the proportion of amorphous phase in the nanocomposite structure with a well-defined morphology [30]. This behavior agreed with the high calcination temperature of the TiO_2-ZnO nanocomposite that influenced the dye adsorption and also the dye decolorization by photocatalysis [31]. In this context, the MnO-Fe_2O_3 nanocomposite prepared at a higher calcination temperature (1100 °C) was chosen to evaluate its efficiency for the removal of cesium and cobalt from contaminated aqueous solutions, as illustrated in the following experiments.
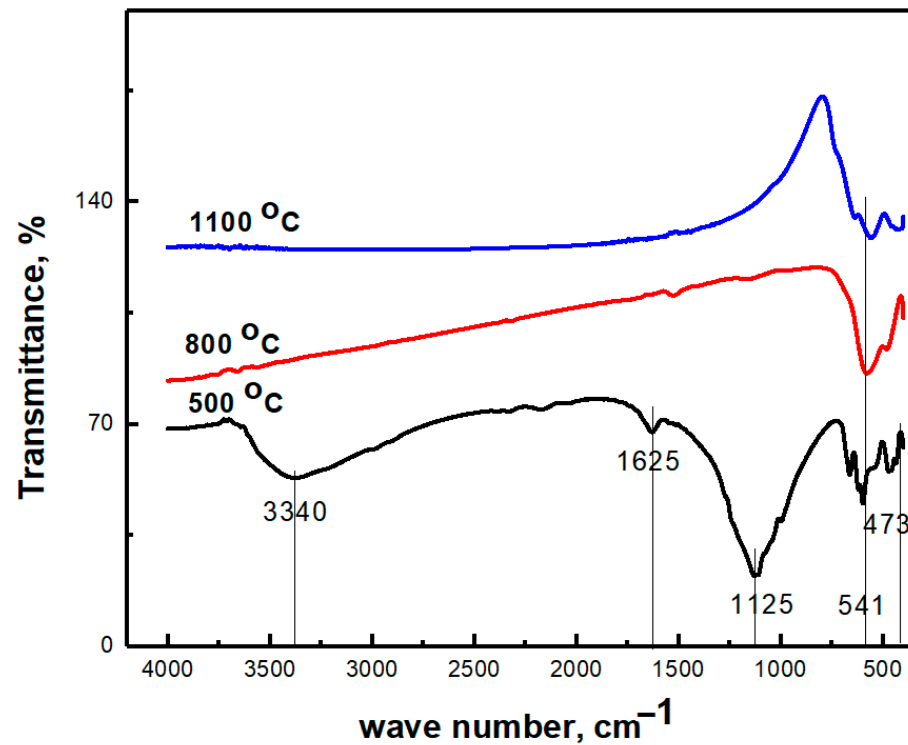

Figure 4. FTIR spectra of synthesized MnO-Fe_2O_3 composites at temperatures of 500, 800, and 1100 °C.
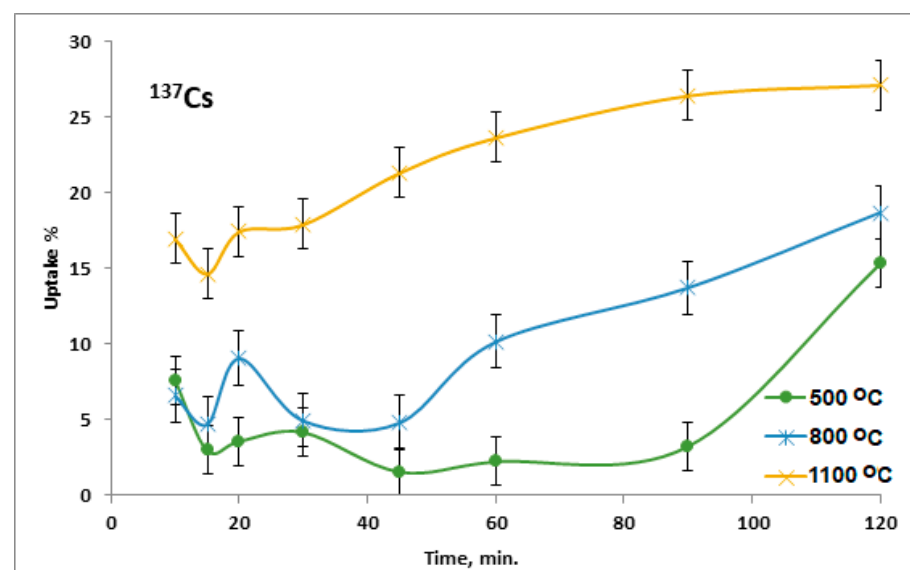

Figure 5. Effect of calcination temperature of nanocomposites on the sorption efficiency of ^{137}Cs from aqueous solution.

3.2.2. Impact of Contact Time on ^{137}Cs and ^{60}Co Removal

Based on the spectroscopic analyses including SEM, XRD, and FTIR and the preliminary experiment performed with ^{137}Cs, it could be confirmed that the nanocomposite produced at 1100 °C is more suitable for adsorption technique according to its morphological structure and porous surface. To establish the optimal equilibrium time for achieving maximum sorption efficiency and to comprehend the kinetics of the sorption of ^{137}Cs and ^{60}Co by the MnO-Fe$_2$O$_3$ nanocomposite, an investigation was conducted by varying the contact time. Figure 6 illustrates the influence of contact time on the sorption of ^{137}Cs and ^{60}Co by the MnO-Fe$_2$O$_3$ nanocomposite from an aqueous solution at various initial radioactivity contents ranging from 1 to 2.46 Bq for ^{60}Co and from 19.5 to 55 Bq for ^{137}Cs.
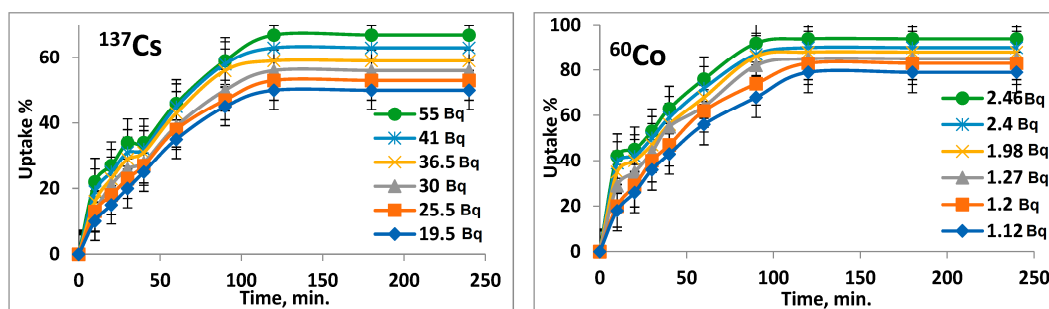

Figure 6. Effect of contact time on the sorption efficiency of ^{137}Cs and ^{60}Co by MnO-Fe$_2$O$_3$ nanocomposite from aqueous solution.

The outcomes revealed a remarkably swift sorption process for both ^{137}Cs and ^{60}Co by the MnO-Fe$_2$O$_3$ nanocomposite. Equilibrium was effectively attained within approximately 100 min for both cations. This finding underscores the rapid nature of the sorption process. Consequently, a contact time of 100 min was deemed adequate for efficient sorption and thus was adopted for all subsequent experiments.

3.2.3. Effect of Dose Amount on Removal of ^{137}Cs and ^{60}Co

In order to optimize the adsorption of Cs and Co ions, the quantity of nanomaterial adsorbent was systematically adjusted within the range of 0.012 to 0.25 g, as depicted in Figure 7. Evidently, the results highlighted that a dose of 0.2 g of adsorbent (nanocomposite) proved to be sufficient for achieving maximum removal of both ions. At this juncture, the adsorption of Cs or Co ions reached its optimal capacity, with only a marginal further increment observed as the adsorbent dose increased. This slight increase can be attributed to the heightened availability of adsorption sites on the adsorbent due to a larger free surface area.

Maintaining a constant concentration of metal ions, the adsorption capacity exhibited an upward trend in correlation with the augmented availability of adsorption sites stemming from the increased surface area of the adsorbent. Conversely, as the concentration of ions bound to the adsorbent sites increased, the adsorption capacity gradually declined due to the reduction in available sites. This phenomenon is attributed to the eventual saturation of adsorption sites. Furthermore, at higher concentrations of adsorbed ions, the ratio of the initial number of ion molecules to the accessible adsorption sites increased, resulting in a reduction in adsorption capacity [32].

3.2.4. Effect of Temperature on Removal of ^{137}Cs and ^{60}Co

The significant influence of temperature fluctuations on the sorption process is widely recognized. In light of this, a series of experiments at temperatures of 25, 35, 45, and 55 °C were systematically undertaken to comprehensively examine the impact of temperature on the sorption process (Figure 8). Precisely, the sorption characteristics of 4 g/L of ^{137}Cs and ^{60}Co ions were investigated.
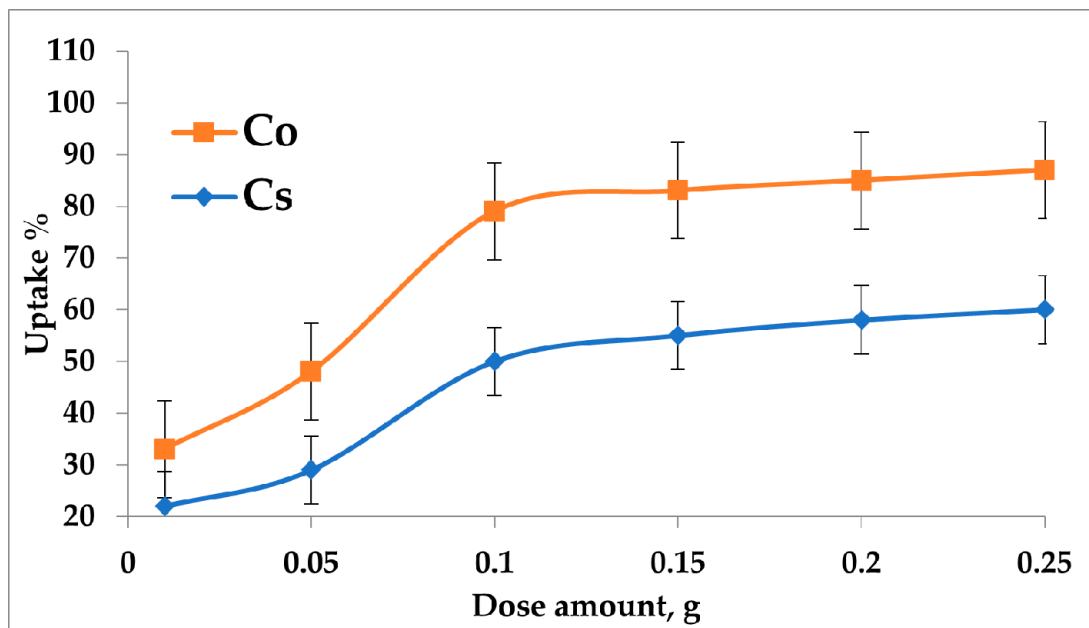
Figure 7. Effect of dose amount on the sorption efficiency of ^{137}Cs and ^{60}Co by MnO-Fe$_2$O$_3$ nanocomposite from aqueous solution.
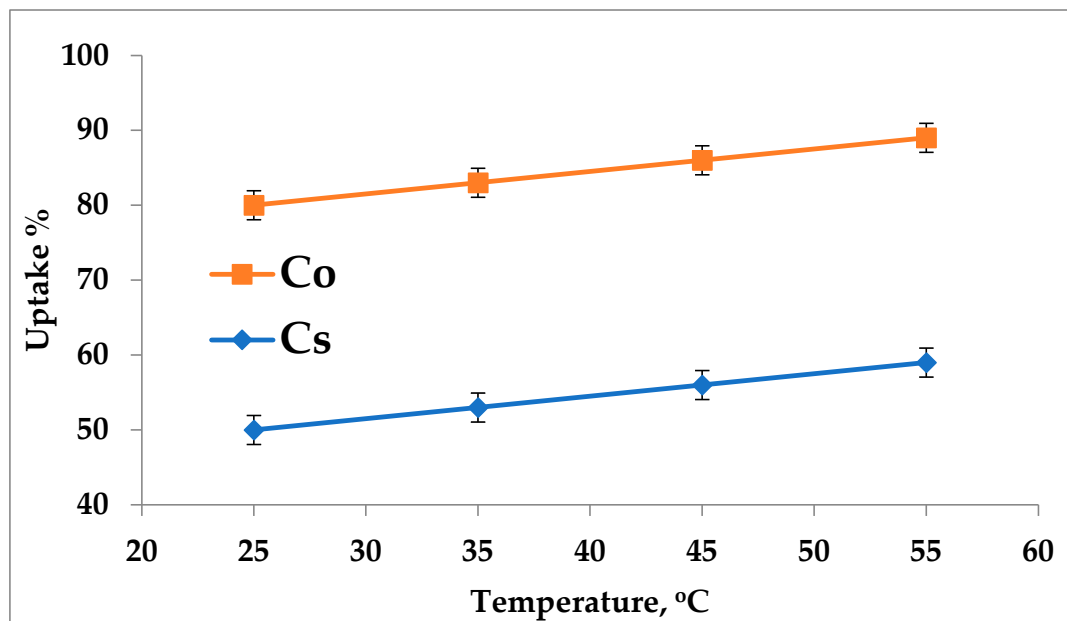

Figure 8. Influence of temperature on sorption efficiency of ^{137}Cs and ^{60}Co by MnO-Fe$_2$O$_3$ nanocomposite from aqueous solution.

The effect of different temperatures on the removal percentage and the amounts of both radioisotopes sorbed from their aqueous solutions was conducted at the optimal contact time and constant initial activity contents. The sorbed amounts and the associated removal of ^{60}Co were greater than those of ^{137}Cs, with a positive effect of temperature reflecting the endothermic natures of sorption [33]. During contact time at different temperatures, about 89% and 59% of the sorbed amounts were reached for ^{60}Co and ^{137}Cs, respectively. This may be due to the higher availability of both metal ions around the MnO-Fe$_2$O$_3$ nanocomposite during contact time.

3.2.5. Effect of pH-Value on Removal of ^{137}Cs and [60]Co

Due to its impact on the surface of the adsorbent and the ionic form of the metal ion in an aqueous solution, the pH value of the solution is a crucial dominating parameter in sorption processes [34]. The effect of the initial pH value on the removal efficiency of ^{137}Cs and ^{60}Co by the MnO-Fe$_2$O$_3$ nanocomposite from an aqueous solution was followed as shown in Figure 9. The removal efficiency was firstly increased when increasing the initial pH value up to 8 and 9 for ^{60}Co and ^{137}Cs, respectively; then, it nearly attained a constant value when the pH value was further increased. The pH value of the solution affects the surface charge of the adsorbent and the chemical speciation of both adsorbates.
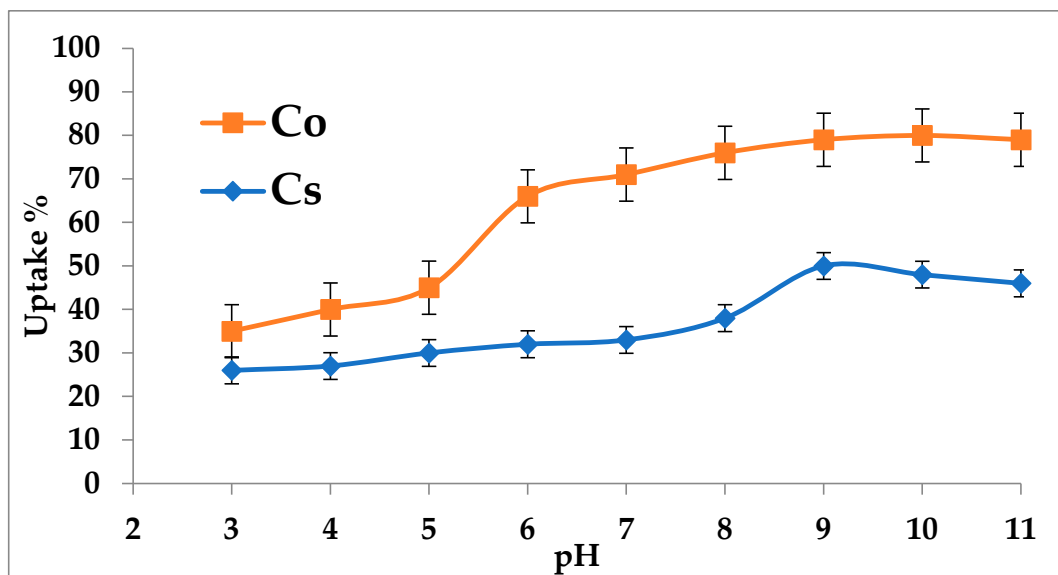

Figure 9. Effect of pH value on the sorption efficiency of ^{137}Cs and ^{60}Co by MnO-Fe$_2$O$_3$ nanocomposite from aqueous solution.

The uptake percentages of ^{137}Cs were increased by raising the pH value from 3 to 9. This is due to the fact that H$_3$O$^+$ had a large concentration at lower pH values and competed with cesium ions for free active sites [35]. With increasing pH value, the concentration of H$_3$O$^+$ decreased and the deprotonation of the active site on the adsorbent surface increased, thus enabling these sites to attract cesium ions and hence the uptake of cesium increased. At higher pH values, the uptake was slightly decreased when increasing pH value up to 11 [36].

On the other hand, the uptake of ^{60}Co increased by a lot when the pH value increased from 3 up to 6 and increased slightly when pH increased from 6 to 9, then reached equilibrium, and remained constant when the pH value increased up to 11. At pH values higher than 6.5, the removal was attributed to the precipitation of ^{60}Co and the presence of Co(OH)$_2$ as the predominant species [37].

3.2.6. Kinetic Studies

Figures 10–15 and Table 1 provide an in-depth illustration of the kinetic studies. These investigations were geared towards determining the underlying mechanisms governing sorption behavior. To probe these mechanisms, the pseudo-first-order (PFO) and pseudo-second-order (PSO) rate equations were employed to analyze the experimental sorption data.
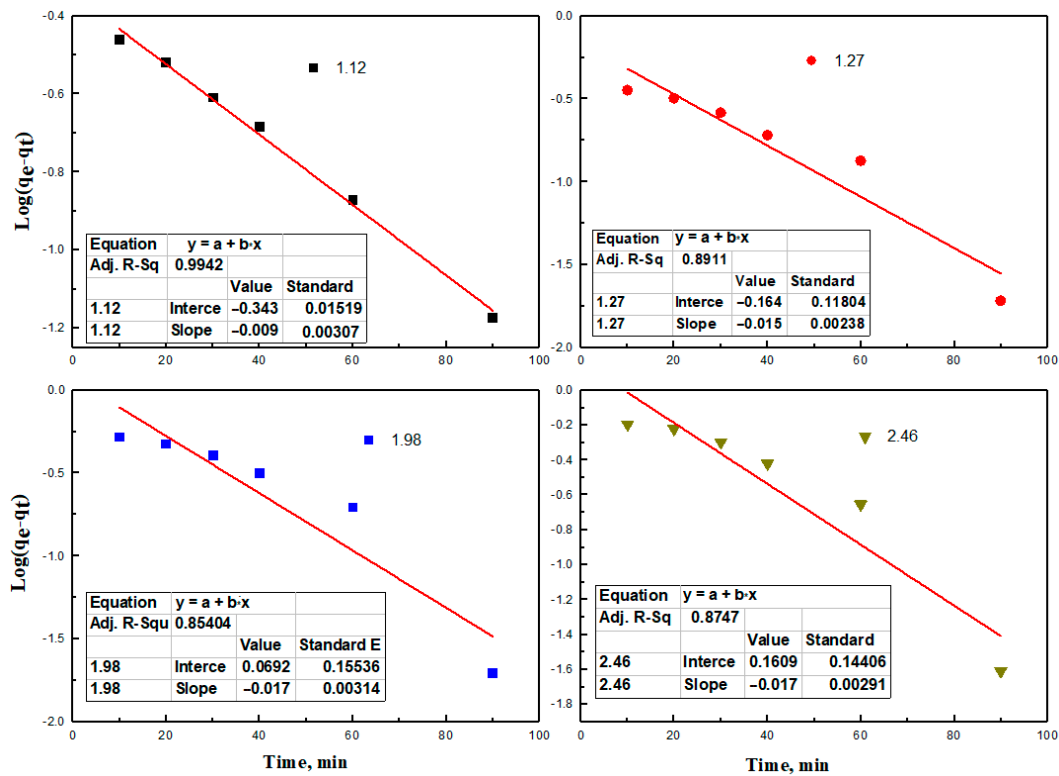
Figure 10. Pseudo-first-order sorption kinetics of adsorption of ^{60}Co on MnO-Fe$_2$O$_3$ nanocomposite from aqueous solution.
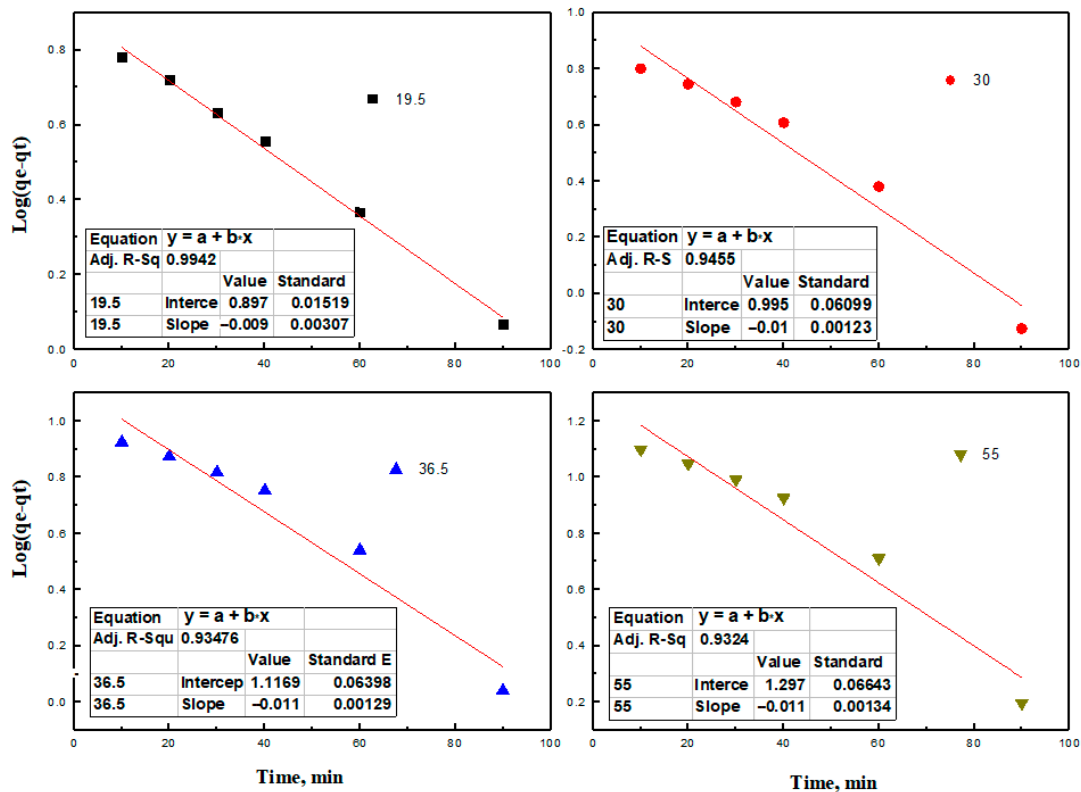

Figure 11. Pseudo-first-order sorption kinetics of adsorption of ^{137}Cs on MnO-Fe$_2$O$_3$ nanocomposite from aqueous solution.

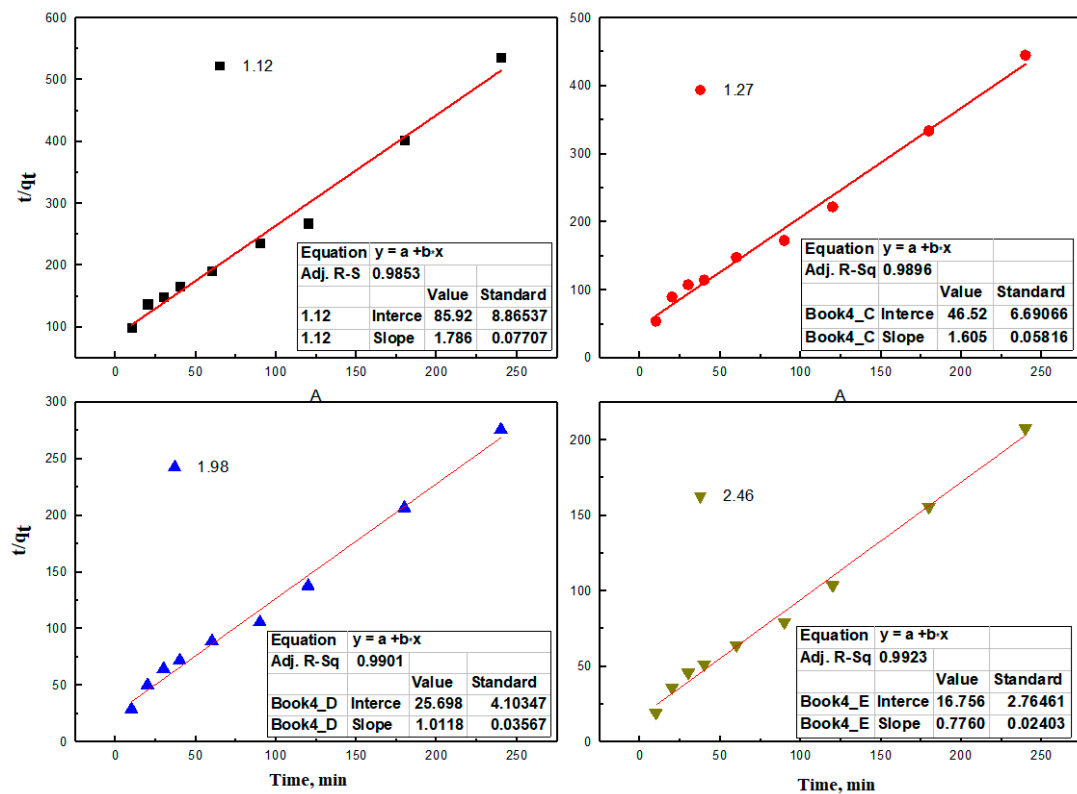**Figure 12.** Pseudo-second-order reaction of adsorption of ^{60}Co on MnO-Fe$_2$O$_3$ nanocomposite from aqueous solution.
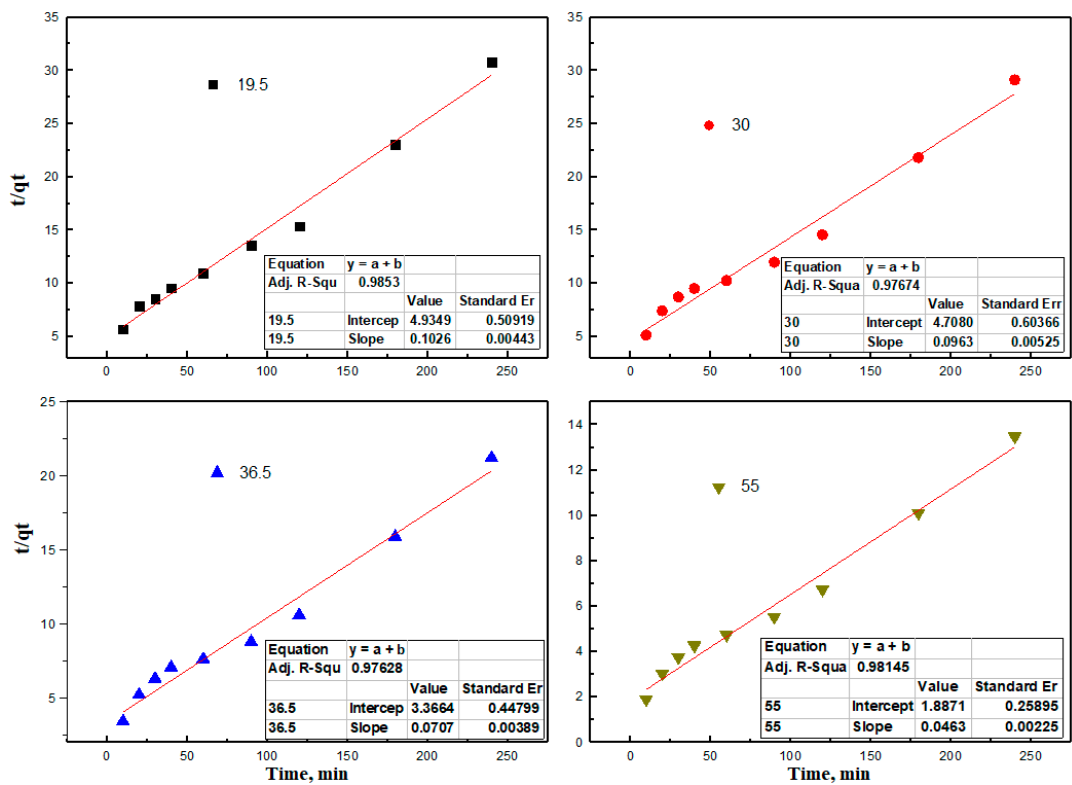

Figure 13. Pseudo-second-order reaction of adsorption of ^{137}Cs on MnO-Fe$_2$O$_3$ nanocomposite from aqueous solution.
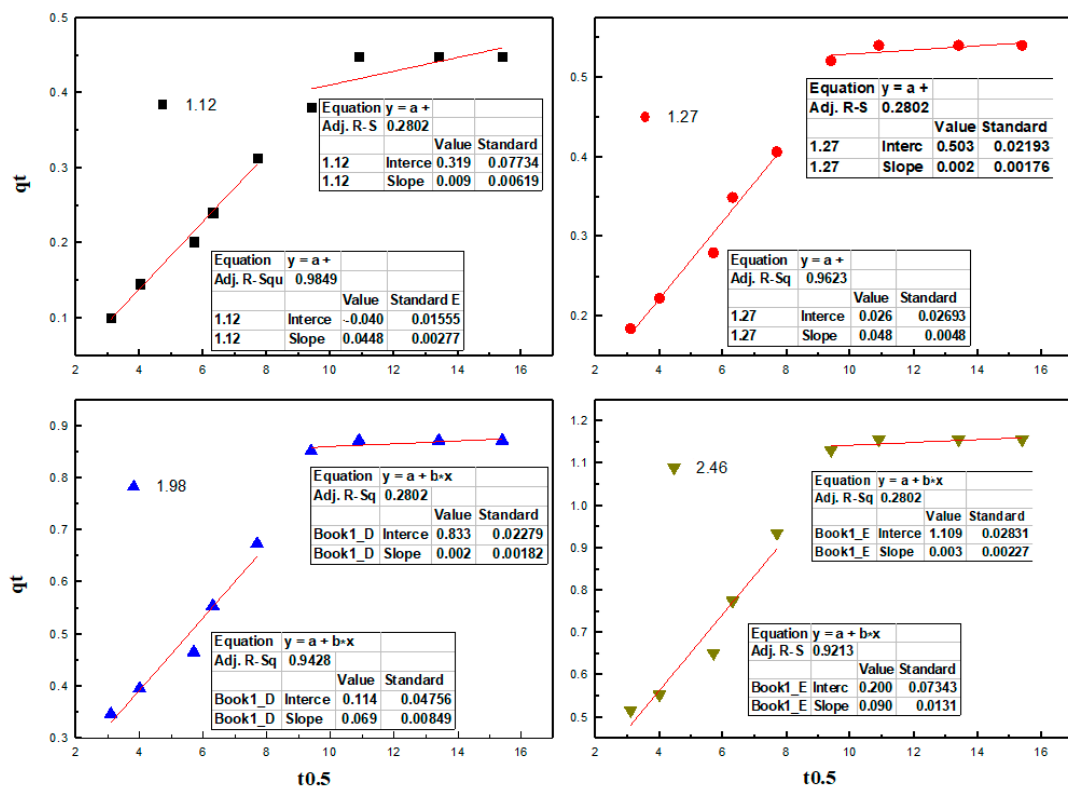
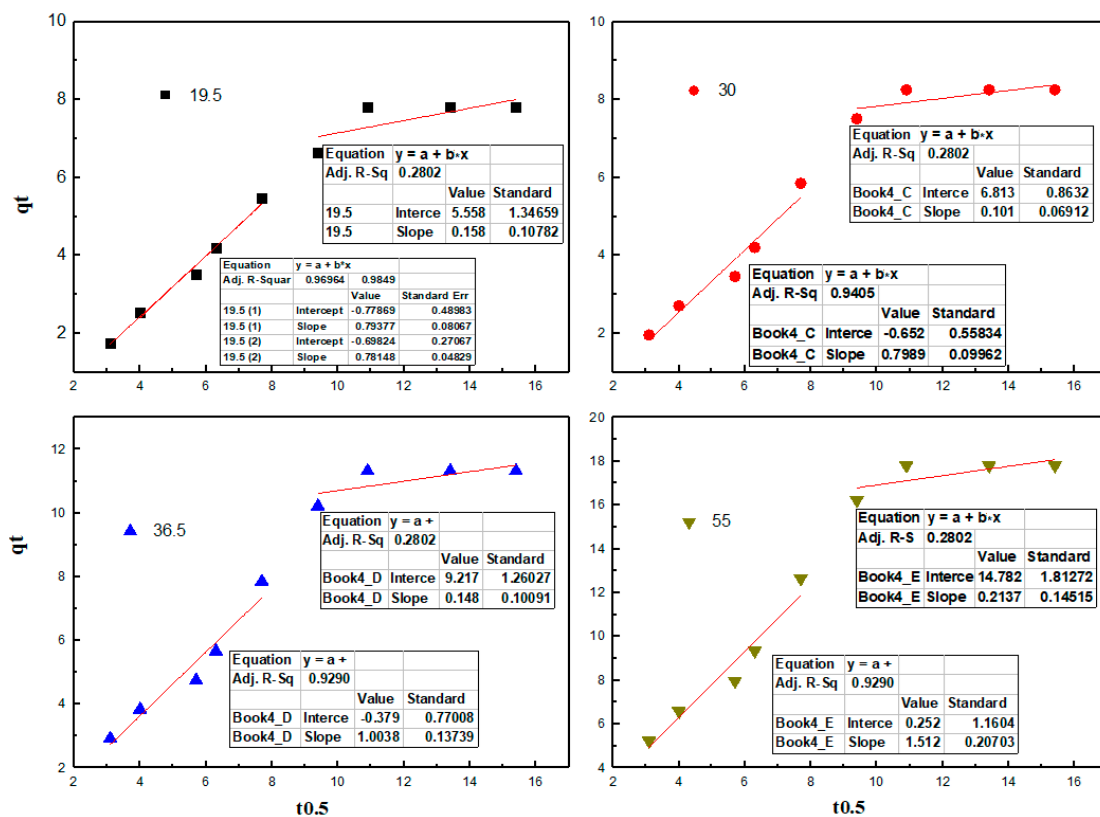**Figure 14.** Morris–Weber plot for adsorption of ^{60}Co on MnO-Fe$_2$O$_3$ nanocomposite from aqueous solution.

Figure 15. Morris–Weber plot for adsorption of ^{137}Cs on MnO-Fe$_2$O$_3$ nanocomposite from aqueous solution.

Table 1. Parameters of kinetic models for the adsorption of ^{137}Cs and ^{60}Co onto MnO-Fe$_2$O$_3$ nanocomposite from aqueous solution.

		^{60}Co				^{137}Cs			
Activity		**1.12**	**1.27**	**1.98**	**2.46**	**19.6**	**30**	**36.5**	**55**
Pseudo-first-order	K$_1$ (min^{-1})	0.012	0.011	0.011	0.017	0.011	0.019	0.013	0.007
	qecal (mg/g)	32.8	34.5	34.5	45.5	34.5	42.1	41.2	29.2
	qeexp (mg/g)	30.3	27.9	27.9	27.6	27.9	30.6	30.0	30.0
	R^2	0.87	0.91	0.91	0.80	0.91	0.93	0.88	0.99
Pseudo-second-order	K$_2$ (min^{-1})	0.00032	0.00008	0.0000	0.00009	0.00008	0.00033	0.00007	0.00011
	qecal (mg/g)	37.7	50.8	50.8	50.3	50.8	39.1	55.6	47.2
	qeexp (mg/g)	30.3	27.9	27.9	27.6	27.9	30.6	30.0	30.0
	R^2	0.98	0.99	0.99	0.97	0.99	0.97	0.97	0.97
Weber and Morris model	Ki (mg min$^{1/2}$)	1.76	1.93	1.93	1.93	1.93	1.84	2.09	1.92
	C	0.9	−4.6	−4.6	−4.5	−4.6	1.2	−4.9	−4.0
	R^2	0.98	0.99	0.99	0.99	0.99	0.96	0.99	0.99

The pseudo-first-order model (PFO), a straightforward framework describing the sorption rate based on sorption capacity, was utilized to explain the kinetics of metal ion sorption onto the adsorbent. The expression for the PFO model is represented by Equation (2):

$$log\ (qe - qt) = log\ qe - (k_1/2.303)\ t \tag{2}$$

Here, k_1 represents the PFO rate constant (min^{-1}), and qe and qt (mg g^{-1}) denote the amounts of metal ion adsorbed at equilibrium and at time t, respectively. Additionally, the PSO model is expressed as Equation (3):

$$\frac{t}{q_t} = \frac{1}{q_e^2 k_2} + \frac{1}{q_e}t \tag{3}$$

Here, k_2 (g mg^{-1} min^{-1}) is the PSO rate constant of adsorption. The validity of the model was checked by calculating the correction coefficient value of straight lines (R^2) as well as consistency between the experimental and calculated values of the PFO model and PSO.

Most adsorption processes entail a multi-step mechanism comprising (i) external film diffusion, (ii) intraparticle diffusion, and (iii) interaction between the adsorbate and active sites [38]. In this study, the agitation of the solution eliminated the external film diffusion step. As a result, the rate-controlling aspect resided within the remaining two steps. The evaluation of intraparticle diffusion was conducted to ascertain whether it acted as the rate-determining step or not, employing the Fickian diffusion equation (Equation (4)):

$$qt = Ki\ t^{0.5} + Xi \tag{4}$$

where qt is the amount of metal ion adsorbed at time t and Ki is the intraparticle diffusion rate (mg g^{-1} min$^{-0.5}$), while Xi represents the boundary layer diffusion effect. As the value of Xi decreases, the effect of external diffusion on the reaction rate decreases.

The Weber–Morris intra-particle diffusion model was employed to explore the likelihood of both intra-particle and liquid-film diffusion mechanisms [39]. To test the linearity of the experimental values, a plot of qt against t 0.5 was utilized. If the plot exhibited linearity and passed through the origin, it indicated that internal diffusion was the slowest (rate-determining) step in the adsorption process. Conversely, if the plot was non-linear or linear but did not intersect the origin, it suggested a potential combined influence of film diffusion and internal diffusion on the adsorption process. It is concluded that the

kinetics of ^{137}Cs and ^{60}Co removal on MnO-Fe$_2$O$_3$ nanocomposites aligned well with the pseudo-second-order model.

3.2.7. Exploration of Adsorption Isotherms

To ascertain the adsorption capacity of the MnO-Fe$_2$O$_3$ nanocomposite for ^{137}Cs and ^{60}Co, adsorption isotherms were conducted at 25 °C and pH 7. The adsorption data related to the interaction of ^{137}Cs and ^{60}Co with the MnO-Fe$_2$O$_3$ nanocomposite in aqueous solutions (as illustrated in Figure 16) were analyzed by fitting them to the Langmuir, Freundlich, and Dubinin–Raduskevich (D-R) isotherms. The derived constants have been computed and are displayed in Table 2. The Langmuir equation takes the form of Equation (5):

$$\frac{1}{q_e} = \frac{1}{k_L q_{max} C_e} + \frac{1}{q_{max}} \tag{5}$$

Here, C_e represents the equilibrium concentration of ion in the solution (mg L^{-1}), qe stands for the adsorbed ion quantity at equilibrium concentration (mg g^{-1}), q_{max} signifies the maximum adsorption capacity (mg g^{-1}), and k_L is the Langmuir binding constant associated with the energy of adsorption (L mg^{-1}). Plotting $1/q_e$ against $1/C_e$ yields a linear relationship, with a slope and intercept equivalent to $1/k_L q_{max}$ and q_{max}, respectively. The calculated values of k_L and q_{max} were determined for ion adsorption at varying temperatures.

Table 2. Thermodynamic parameters for adsorption of radiocobalt ^{60}Co and radiocesium ^{137}Cs on MnO-Fe$_2$O$_3$ nanocomposite from aqueous solution.

Element	T K	ΔH KJ·mol^{-1}	ΔS KJ·mol·k^{-1}	TΔS KJ·mol^{-1}	ΔG KJ·mol^{-1}
^{60}Co	298			−25.628	5.228
	308			−26.488	6.088
	318	−20.4	−0.086	−27.348	6.948
	328			−28.208	7.808
^{137}Cs	298			−11.741	1.3712
	308			−12.135	1.7652
	318	−10.37	−0.0394	−12.529	2.1592
	328			−12.923	2.5532

The q_{max} values derived from the Langmuir plots are largely in agreement with the experimental values. This observation suggests that the adsorption process predominantly follows a monolayer mechanism and adheres to the Langmuir isotherm across all conditions. The degree of suitability of the adsorbent towards ions was estimated from the values of the separation factor (R_L) (Equation (6)).

$$R_L = \frac{1}{1 + K_L C_o} \tag{6}$$

Here, K_L represents the Langmuir equilibrium constant, and C_o indicates the initial concentration of the metal ion. R_L values within the range of 0 to 1 indicate the suitability of the process. The Freundlich equation is expressed as Equation (7):

$$\ln q_e = \ln K_f + \frac{1}{n} \ln C_e \tag{7}$$

$\ln q_e$ was plotted against $\ln C_e$, with the slope and intercept at $1/n$ and $\ln K_f$, respectively, where C_e is the equilibrium concentration of the metal ion solution (mg L^{-1}), $qe$is is the amount of adsorbed metal ion at equilibrium (mg g^{-1}), K_f (mg$^{1-1/n}$ L$^{1/n}$ g^{-1}) is the Freundlich constant for the adsorption capacity, and n is the adsorption intensity. It is noteworthy that the data exhibited good fits with both the Langmuir and Freundlich isotherms, as evidenced by high correlation coefficients (R^2) at 25 °C.
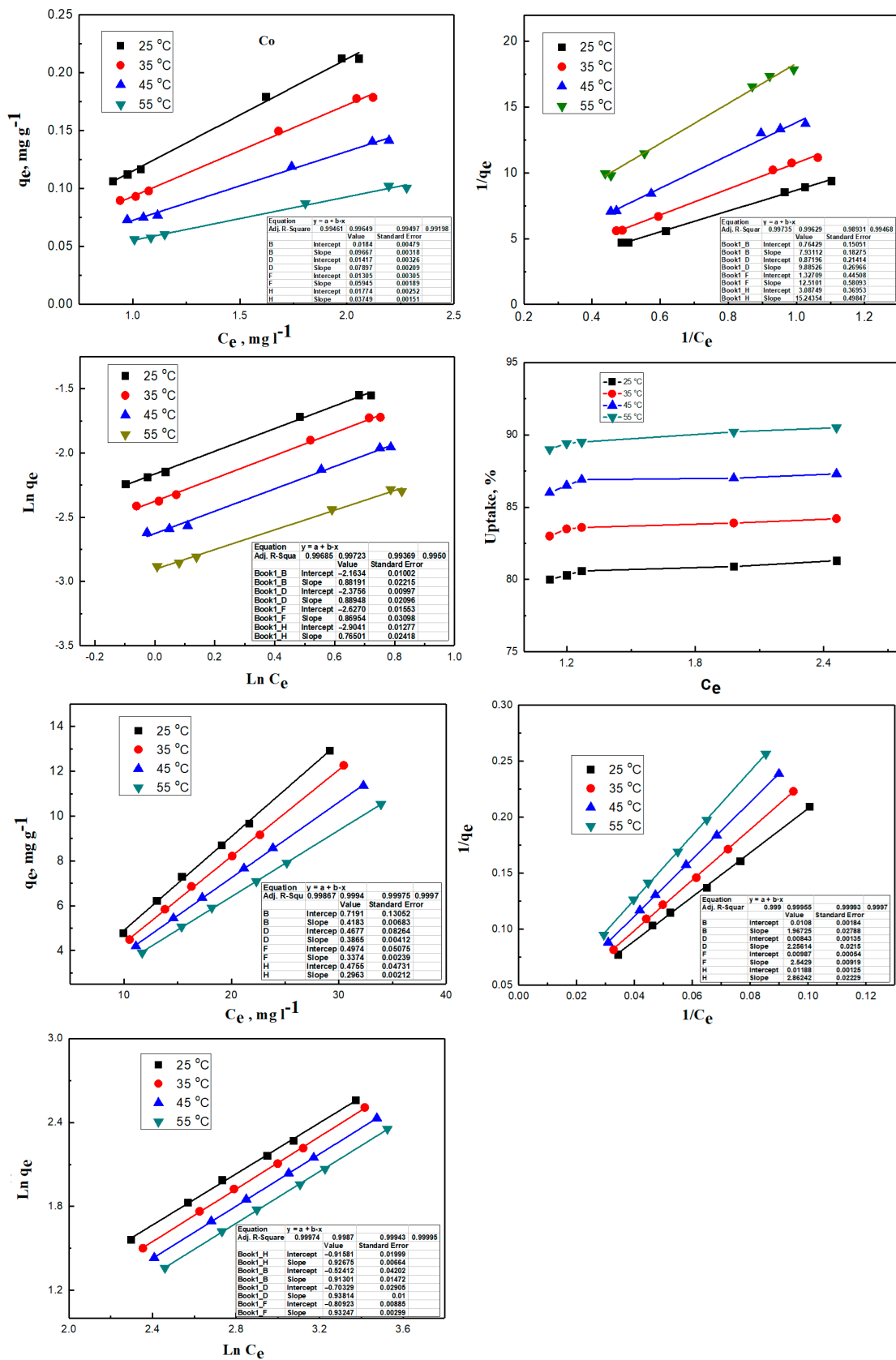
Figure 16. Adsorption data for ^{137}Cs and ^{60}Co adsorption on MnO-Fe$_2$O$_3$ nanocomposite from aqueous solution—Langmuir, Freundlich, and Dubinin–Raduskevich (D-R) isotherms.

3.2.8. Thermodynamic Analysis and Adsorption Reaction

As presented in Figure 17 and Table 2, the endeavor to derive the thermodynamic parameters of the adsorption reaction led to the processing of k_L values at varying temperatures, as per the van't Hoff equation (Equation (8)):

$$\ln k_L = \frac{-\Delta H^o}{RT} + \frac{\Delta S^o}{R} \tag{8}$$

Here, ΔH^O (KJ·mol^{-1}) and ΔS^O (KJ·mol·k^{-1}) denote changes in enthalpy and entropy, respectively, while R stands for the gas constant. Plotting k_L against $1/T$ yields a linear relationship, and the slope and intercept represent $\Delta H^O/R$ and $\Delta S^O/R$, respectively. The observed positive value of ΔH^O signifies the endothermic nature of the adsorption process.
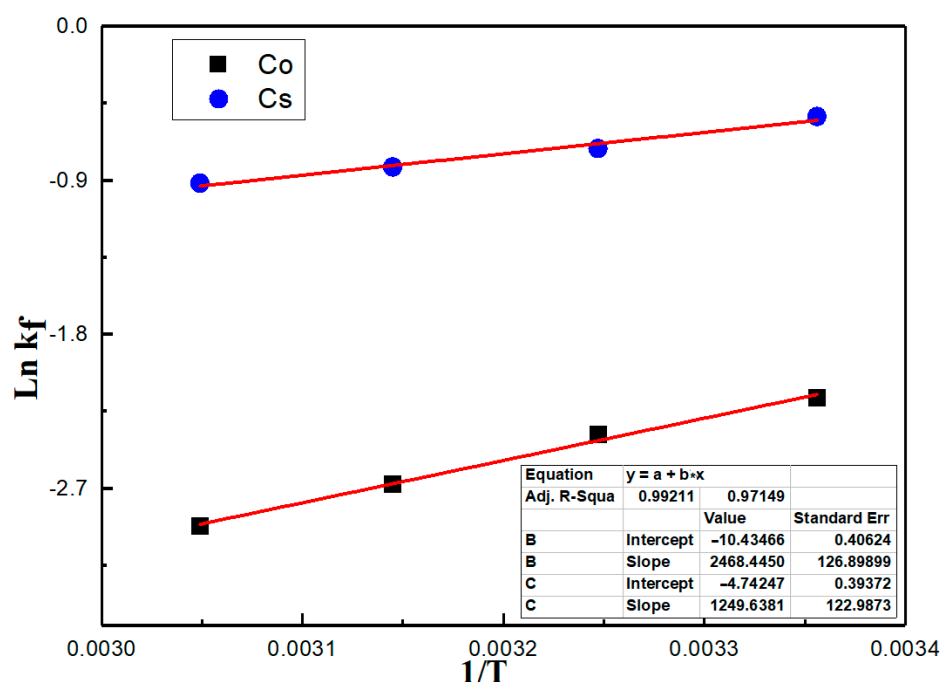

Equation	y = a + b*x		
Adj. R-Squa	0.99211	0.97149	
		Value	Standard Err
B	Intercept	−10.43466	0.40624
B	Slope	2468.4450	126.89899
C	Intercept	−4.74247	0.39372
C	Slope	1249.6381	122.9873

Figure 17. Van't Hoff plots for adsorption of ^{137}Cs and ^{60}Co on MnO-Fe$_2$O$_3$ nanocomposite.

The Gibbs free energy of adsorption (ΔG^O) was computed using the relation defined by Equation (9):

$$\Delta G^O = \Delta H^O - T\Delta S^O \tag{9}$$

The negative values of ΔG^O (KJ·mol^{-1}) indicated that the adsorption reaction is spontaneous and $|T\Delta S^O| > |\Delta H^O|$. This signifies that the adsorption process is predominantly influenced by entropic changes rather than enthalpic alterations. The ΔG^O values that ranged from −20 to 0 KJ·mol^{-1} was attributed to physisorption, while chemisorption was assigned values that ranged from −80 to −400 KJ·mol^{-1}.

If $|T\Delta S^O| < |\Delta H^O|$, this indicated that the adsorption is dominated by enthalpic rather than entropic change. A positive ΔG^O value signifies that the ion adsorption process is nonspontaneous.

4. Conclusions

In this paper, MnO-Fe$_2$O$_3$ nanocomposites were used as adsorbents for ^{60}Co and ^{137}Cs removal from radioactive waste. Through a rigorous analysis of the empirical data gathered from the experiments, it was evident that the removal process was notably affected by the solution's pH value. The optimal operating conditions were determined to be as follows: a pH value of 6, an adsorbent particle size of 0.0425 μm, and an adsorbent dosage set to 4 g/L.

The Langmuir isotherm emerged as the best-fitting model for describing the equilibrium data for removal of ^{137}Cs and ^{60}Co by MnO-Fe$_2$O$_3$ nanocomposites. Furthermore, it was observed that the kinetics of ^{137}Cs and ^{60}Co removal on MnO-Fe$_2$O$_3$ nanocomposites aligned well with the pseudo-second-order model. In forthcoming research, the efficiency of the proposed promising nanocomposite in the treatment of other toxics elements such as heavy metals will be pursued.

References

1. Mushtaq, W.; Rafiq, M.; Mushtaq, Z.; Nadeem, F.; Abdul, H. Wastewater Treatment and Dye Sequestration Using Potential Magnetic Composites—A Comprehensive Review. *Int. J. Chem. Biochem. Sci.* **2019**, *15*, 74–86.
2. Allan, K.F.; Holiel, M.; Sanad, W.A. Gamma Radiation Induced Preparation of Organic-Inorganic Composite Material for Sorption of Cesium and Zinc. *Radiochemistry* **2014**, *56*, 267–274. [CrossRef]
3. Mansy, M.S.; Hassan, R.S.; Selim, Y.T.; Kenawy, S.H. Evaluation of Synthetic Aluminum Silicate Modified by Magnesia for the Removal of 137Cs, 60Co and 152+ 154Eu from Low-Level Radioactive Waste. *Appl. Radiat. Isot.* **2017**, *130*, 198–205. [CrossRef]
4. Ma, B.; Shin, W.S.; Oh, S.; Park, Y.-J.; Choi, S.-J. Adsorptive Removal of Co and Sr Ions from Aqueous Solution by Synthetic Hydroxyapatite Nanoparticles. *Sep. Sci. Technol.* **2010**, *45*, 453–462. [CrossRef]
5. IAEA. *Management of Low and Intermediate Level Radioactive Wastes with Regard to Their Chemical Toxicity*; TECDOC Series 1325; International Atomic Energy Agency: Vienna, Austria, 2003; ISBN 92-0-119802-7.
6. Razzak, S.A.; Faruque, M.O.; Alsheikh, Z.; Alsheikhmohamad, L.; Alkuroud, D.; Alfayez, A.; Hossain, S.M.Z.; Hossain, M.M. A Comprehensive Review on Conventional and Biological-Driven Heavy Metals Removal from Industrial Wastewater. *Environ. Adv.* **2022**, *7*, 100168. [CrossRef]
7. Dawoud, M.M.A.; Hegazi, M.M.; Saleh, H.M.; El Helew, W.K. Removal of Stable and Radio Isotopes from Wastewater by Using Modified Microcrystalline Cellulose Based on Taguchi L16. *Int. J. Environ. Sci. Technol.* **2022**, *20*, 1289–1300. [CrossRef]
8. Abdelhamid, A.A.; Badr, M.H.; Mohamed, R.A.; Saleh, H.M. Using Agricultural Mixed Waste as a Sustainable Technique for Removing Stable Isotopes and Radioisotopes from the Aquatic Environment. *Sustainability* **2023**, *15*, 1600. [CrossRef]
9. Eskander, S.B.; Saleh, H.M.; Tawfik, M.E.; Bayoumi, T.A. Towards Potential Applications of Cement-Polymer Composites Based on Recycled Polystyrene Foam Wastes on Construction Fields: Impact of Exposure to Water Ecologies. *Case Stud. Constr. Mater.* **2021**, *15*, e00664. [CrossRef]
10. Saleh, H.M.; Moussa, H.R.; El-Saied, F.A.; Dawoud, M.; Bayoumi, T.A.; Abdel Wahed, R.S. Mechanical and Physicochemical Evaluation of Solidified Dried Submerged Plants Subjected to Extreme Climatic Conditions to Achieve an Optimum Waste Containment. *Prog. Nucl. Energy* **2020**, *122*, 103285. [CrossRef]
11. Saleh, H.M.; Bondouk, I.I.; Salama, E.; Esawii, H.A. Consistency and Shielding Efficiency of Cement-Bitumen Composite for Use as Gamma-Radiation Shielding Material. *Prog. Nucl. Energy* **2021**, *137*, 103764. [CrossRef]
12. Singh, S.; Eapen, S.; Thorat, V.; Kaushik, C.P.; Raj, K.; D'souza, S.F. Phytoremediation of 137cesium and 90strontium from Solutions and Low-Level Nuclear Waste by Vetiveria Zizanoides. *Ecotoxicol. Environ. Saf.* **2008**, *69*, 306–311. [CrossRef]
13. Abdel Ghaffar, A.M.; El-Arnaouty, M.B.; Diab, H.M.; Hegazy, E.-S.A. Radiation Synthesis of Grafted Polymers for Studying Thermoluminescence Characterization and Its Possible Application as a Dosimeter at Low Doses. *Polym. Plast. Technol. Eng.* **2009**, *48*, 423–431. [CrossRef]
14. Afifi, M.; Abass, M.R.; Diab, H.M.; Abou-Mesalam, M.M.; Gaafar, M.S. Dosimetric Impact of Some Gamma Radiation-Induced Polymeric Materials Incorporated Silicate Using Thermoluminescence and Ultrasonic Techniques. *Silicon* **2022**, *14*, 4391–4400. [CrossRef]
15. Hao, W.M.; Baker, S.; Lincoln, E.; Hudson, S.; Lee, S.D.; Lemieux, P. Cesium Emissions from Laboratory Fires. *J. Air Waste Manag. Assoc.* **2018**, *68*, 1211–1223. [CrossRef]
16. Zhang, L.; Wei, J.; Zhao, X.; Li, F.; Jiang, F.; Zhang, M.; Cheng, X. Competitive Adsorption of Strontium and Cobalt onto Tin Antimonate. *Chem. Eng. J.* **2016**, *285*, 679–689. [CrossRef]

17. Corami, A.; Mignardi, S.; Ferrini, V. Cadmium Removal from Single-and Multi-Metal (Cd+ Pb+ Zn+ Cu) Solutions by Sorption on Hydroxyapatite. *J. Colloid Interface Sci.* **2008**, *317*, 402–408. [CrossRef]

18. Krestou, A.; Xenidis, A.; Panias, D. Mechanism of Aqueous Uranium (VI) Uptake by Hydroxyapatite. *Miner. Eng.* **2004**, *17*, 373–381. [CrossRef]

19. Hamed, M.M.; Holiel, M.; Ahmed, I.M. Sorption Behavior of Cesium, Cobalt and Europium Radionuclides onto Hydroxyl Magnesium Silicate. *Radiochim. Acta* **2016**, *104*, 873–890. [CrossRef]

20. El-Aryan, Y.F.; El-Said, H.; Abdel-Galil, E.A. Synthesis and Characterization of Polyaniline-Titanium Tungstophosphate; Its Analytical Applications for Sorption of Cs^+, Co^{2+}, and Eu^{3+} from Waste Solutions. *Radiochemistry* **2014**, *56*, 614–621. [CrossRef]

21. Faghihian, H.; Iravani, M.; Moayed, M.; Ghannadi-Maragheh, M. Preparation of a Novel PAN–Zeolite Nanocomposite for Removal of Cs^+ and Sr^{2+} from Aqueous Solutions: Kinetic, Equilibrium, and Thermodynamic Studies. *Chem. Eng. J.* **2013**, *222*, 41–48. [CrossRef]

22. Li, Y.-H.; Di, Z.; Ding, J.; Wu, D.; Luan, Z.; Zhu, Y. Adsorption Thermodynamic, Kinetic and Desorption Studies of Pb^{2+} on Carbon Nanotubes. *Water Res.* **2005**, *39*, 605–609. [CrossRef]

23. Navas, D.; Fuentes, S.; Castro-Alvarez, A.; Chavez-Angel, E. Review on Sol-Gel Synthesis of Perovskite and Oxide Nanomaterials. *Gels* **2021**, *7*, 275. [CrossRef]

24. Celebi, O.; Kilikli, A.; Erten, H.N. Sorption of Radioactive Cesium and Barium Ions onto Solid Humic Acid. *J. Hazard. Mater.* **2009**, *168*, 695–703. [CrossRef]

25. Hashemian, S. MnFe2O4/Bentonite Nano Composite as a Novel Magnetic Material for Adsorption of Acid Red 138. *Afr. J. Biotechnol.* **2010**, *9*, 8667–8671.

26. Faghihian, H.; Moayed, M.; Firooz, A.; Iravani, M. Evaluation of a New Magnetic Zeolite Composite for Removal of Cs^+ and Sr^{2+} from Aqueous Solutions: Kinetic, Equilibrium and Thermodynamic Studies. *Comptes Rendus Chim.* **2014**, *17*, 108–117. [CrossRef]

27. Kim, S.; Gupta, N.K.; Bae, J.; Kim, K.S. Fabrication of Coral-like Mn_2O_3/Fe_2O_3 Nanocomposite for Room Temperature Removal of Hydrogen Sulfide. *J. Environ. Chem. Eng.* **2021**, *9*, 105216. [CrossRef]

28. Gupta, N.K.; Ghaffari, Y.; Kim, S.; Bae, J.; Kim, K.S.; Saifuddin, M. Photocatalytic Degradation of Organic Pollutants over MFe_2O_4 (M= Co, Ni, Cu, Zn) Nanoparticles at Neutral PH. *Sci. Rep.* **2020**, *10*, 4942. [CrossRef]

29. Slatineanu, T.; Diana, E.; Nica, V.; Oancea, V.; Caltun, O.; Iordan, A.; Palamaru, M. The Influence of the Chelating/Combustion Agents on the Structure and Magnetic Properties of Zinc Ferrite. *Open Chem.* **2012**, *10*, 1799–1807. [CrossRef]

30. Mioduska, J.; Zielińska-Jurek, A.; Janczarek, M.; Hupka, J. The Effect of Calcination Temperature on Structure and Photocatalytic Properties of WO_3/TiO_2 Nanocomposites. *J. Nanomater.* **2016**, *2016*, 3145912. [CrossRef]

31. Yu, J.; Yu, H.; Cheng, B.; Trapalis, C. Effects of Calcination Temperature on the Microstructures and Photocatalytic Activity of Titanate Nanotubes. *J. Mol. Catal. A Chem.* **2006**, *249*, 135–142. [CrossRef]

32. SenthilKumar, P.; Ramalingam, S.; Sathyaselvabala, V.; Kirupha, S.D.; Sivanesan, S. Removal of Copper (II) Ions from Aqueous Solution by Adsorption Using Cashew Nut Shell. *Desalination* **2011**, *266*, 63–71. [CrossRef]

33. El-Naggar, M.R.; El-Naggar, I.M.; El-Shahat, M.F.; Abd El-Mohsen, E.S. Sorption of Cesium and Cobalt Ions onto Novel Zirconium Silicophosphate/Polyacrylamide Nanocomposite. *J. Radiat. Res. Appl. Sci.* **2019**, *12*, 319–331. [CrossRef]

34. Sheha, R.; Roushdy, A.; Al-Shazly, E.; Salah, B.; Kandil, A.-E.T.; Kandil, A.-E.T. Investigating the Sorption Behavior of Cesium and Cobalt on Soil Samples. *Arab J. Nucl. Sci. Appl.* **2020**, *53*, 1–12. [CrossRef]

35. Olatunji, M.A.; Khandaker, M.U.; Mahmud, E.H.N.M.; Amin, Y.M.; Ademola, J.A.; Olorode, D.O. Remediation of 137 Cs Radionuclide in Nuclear Waste Effluents by Polymer Composite: Adsorption Kinetics, Isotherms and Gamma Irradiation Studies. *J. Radioanal. Nucl. Chem.* **2018**, *316*, 933–945. [CrossRef]

36. Khandaker, S.; Toyohara, Y.; Kamida, S.; Kuba, T. Effective Removal of Cesium from Wastewater Solutions Using an Innovative Low-Cost Adsorbent Developed from Sewage Sludge Molten Slag. *J. Environ. Manag.* **2018**, *222*, 304–315. [CrossRef] [PubMed]

37. Tewari, P.H.; Campbell, A.B.; Lee, W. Adsorption of Co^{2+} by Oxides from Aqueous Solution. *Can. J. Chem.* **1972**, *50*, 1642–1648. [CrossRef]

38. Sahoo, T.R.; Prelot, B. Adsorption Processes for the Removal of Contaminants from Wastewater: The Perspective Role of Nanomaterials and Nanotechnology. In *Nanomaterials for the Detection and Removal of Wastewater Pollutants*; Elsevier: Amsterdam, The Netherlands, 2020; pp. 161–222.

39. Hwang, K.-J.; Shim, W.-G.; Kim, Y.; Kim, G.; Choi, C.; Kang, S.O.; Cho, D.W. Dye Adsorption Mechanisms in TiO_2 Films, and Their Effects on the Photodynamic and Photovoltaic Properties in Dye-Sensitized Solar Cells. *Phys. Chem. Chem. Phys.* **2015**, *17*, 21974–21981. [CrossRef]